



City Research Online

City, University of London Institutional Repository

Citation: Ghosh, S. & Rahman, B. M. A. (2019). Design of On-chip Hybrid Plasmonic Mach-Zehnder Interferometer for Temperature and Concentration Detection of Chemical Solution. *Sensors and Actuators B: Chemical*, 279, pp. 490-502. doi: 10.1016/j.snb.2018.09.070

This is the accepted version of the paper.

This version of the publication may differ from the final published version.

Permanent repository link: <https://openaccess.city.ac.uk/id/eprint/20978/>

Link to published version: <https://doi.org/10.1016/j.snb.2018.09.070>

Copyright: City Research Online aims to make research outputs of City, University of London available to a wider audience. Copyright and Moral Rights remain with the author(s) and/or copyright holders. URLs from City Research Online may be freely distributed and linked to.

Reuse: Copies of full items can be used for personal research or study, educational, or not-for-profit purposes without prior permission or charge. Provided that the authors, title and full bibliographic details are credited, a hyperlink and/or URL is given for the original metadata page and the content is not changed in any way.

City Research Online:

<http://openaccess.city.ac.uk/>

publications@city.ac.uk

Design of On-chip Hybrid Plasmonic Mach-Zehnder Interferometer for Temperature and Concentration Detection of Chemical Solution

Souvik Ghosh and B. M. A. Rahman

School of Mathematics, Computer Science, and Engineering, City, University of London, UK

*Corresponding Author, souvik.ghosh.1@city.ac.uk

Tel: +44-7405137454

Highlights

- A novel metal strip loaded horizontal slot hybrid plasmonic waveguide with a refractometric sensitivity of 1.13 is proposed.
- Optimized waveguide design shows a high 59.23% and 82.04% quasi-TM field confinement in the slot and sensing (slot + clad) region, respectively.
- A compact Mach-Zehnder interferometer is designed for detection of temperature and volume concentration of isopropanol/water solution, although it is also suitable for any other liquid chemical.
- Asymmetric power splitting scheme **enhances** the interference fringe visibility to the ideal value ($F' \simeq 1$).
- A single on-chip sensor design shows a high temperature sensitivity of 243.9 pm/°C and volume concentration sensitivity of 437.3 nm/RIU.
- The device incorporates a simple design scheme which is highly resilient to the fabrication tolerances.

Keywords

Hybrid plasmonic waveguide, Slot waveguide, Mach-Zehnder interferometer, Integrated optical sensor, Temperature sensor, Chemical sensor

Abstract

We report a compact lab-on-chip design of a Mach-Zehnder interferometer (MZI) incorporating a novel metal strip loaded horizontal slot hybrid plasmonic waveguide (HSHPW) in the sensing arm and a dielectric horizontal slot (DHS) waveguide in the reference arm. The HSHPW is optimized to confine a high ~60% and ~82% evanescent optical field in the low index dielectric slot and an active sensing region, respectively which enhance the device sensitivity with a comparative lower propagation loss than a typical plasmonic waveguide. We report here a single MZI configuration which not only exhibits an excellent temperature sensitivity of 243.9 pm/°C but also liquid concentration sensitivity of 437.3 nm/RIU for a 40 μm long HSHPW. To mitigate loss arising from each section such as butt coupling and plasmonic modal losses, the HSHPW has been optimized by incorporating an asymmetric power splitter which shows a considerable improvement in the fringe visibility and device insertion loss. Thus, the proposed single MZI design shows an excellent response to the temperature and liquid concentration sensing with a maximum total loss and extinction ratio of 2.56 dB and >25 dB, respectively. A much simpler CMOS friendly compact design is also found to have a great robustness to the fabrication tolerances.

1. Introduction

On-chip integrated photonic and plasmonic waveguides [1 – 4] have great potential in applications for biochemical industries, real-time rapid medical diagnosis, early-stage detection of critical diseases, DNA characterizations, environmental monitoring, food and water quality screening, pharmaceutical industries, particle tracing and tweezing etc. [5 – 8]. Several electronic and mechanical sensors have already been commercialized to achieve these functionalities but with a lower detection accuracy, bulky design and high-power consumption. In recent years, integrated optical technology-based sensors are gaining interests as attractive alternative approaches to the electronic technology due to its immunity from electromagnetic interference (EMI), compact portable lab-on-a-chip scale design for low-cost mass production, suitable for real-time monitoring, low power requirements, remote operation, fast response and above all, a much higher sensitivity for accurate detection of targets even at the atomic level. Monitoring and control of most fundamental parameters of organic, inorganic, and hazardous chemical solution such as temperature and concentration of analytes represent a major concern to the biochemical industries and health organizations for their improvement of manufacturing producibility and protection of public health from hazardous accidents. Instead of the commonly used thermocouple and resistance thermometer, optical temperature sensors are attracting substantial interests. Refractometric based photonic sensors incorporating guiding materials with large thermo-optic coefficients (TOC) are promising in many biochemical applications, such as DNA, RNA, and protein precipitation from aqueous solution [9, 10] and temperature sensitive biochemical characterizations where distinct chemical behaviors depend on a small fractional change in temperature [11].

In recent years, various optical fiber-based device configurations, e.g. fibers with Bragg gratings [12, 13], in-line interferometer [14, 15], graphene assisted microfiber interferometer [16], surface plasmon resonance (SPR) supported fiber sensors [17, 18], and modal interferometers in

microstructured optical fibers (MOFs) [15, 19] have been developed and investigated for temperature monitoring. However, on-chip integrated optical temperature sensors based on ring resonators [20, 21], Fabry-Perrot cavities [22], Bragg reflectors [23, 24], and interferometers [25, 26] have also been demonstrated and are envisaged to be favorable candidates for integration with electronic circuits for lab-on-a-chip information processing and calibration compared with their fiber-optic siblings. All these sensing mechanisms are restricted to a much lower temperature sensitivity of around $\sim 70\text{-}80$ pm/°C. Recently published reports by Guan *et al.* [27] and Zhang *et al.* [28] have demonstrated an improved sensitivity of 172 pm/°C and 162.9 pm/°C for Si/SU-8 hybrid waveguide assisted MZI sensor and Si/SU-8 based photonic crystal nanobeam cavities, respectively. Besides temperature sensing, an accurate detection of chemical concentration is of considerable interest in biomedical research and chemical industries [9, 10, 29, 30]. Different exotic waveguide schemes such as disk [31], ring [32, 33] and straight resonators [34, 35], sub-wavelength gratings [36], and interferometers [37, 38] have also been proposed and evaluated as biochemical sensors depending on the changes of mode effective index (n_{eff}) by homogeneous or bulk sensing and localized or surface sensing. A recent report shows a maximum isopropanol refractometric sensitivity of 160 nm/RIU for a hollow hybrid plasmonic MZI liquid sensor [39].

In this paper, we introduce a novel metal strip loaded horizontal slot hybrid plasmonic waveguide (HSHPW) assisted asymmetric unbalanced Mach-Zehnder interferometer (MZI) with dynamic sensing ability. In HSHPW, a nano-scale low index plasmonic slot region is formed by suspending a high index silicon (Si) slab on top of a thin silver (Ag) layer deposited on silica (SiO_2) buffer layer. The key objective of a sensor design would be to enhance light-matter interactions in the low index slot region to obtain a high waveguide sensitivity to a small refractive index change in the sensing material. Dominant quasi-TE mode of a vertical slot waveguide is highly sensitive to the sidewall roughness caused by the dry-etching fabrication process, which results in high scattering loss. On the other hand, the dominant quasi-TM mode suffers less scattering loss as the horizontal interfaces are relatively smoother due to the wet-etching technology used. Thus, the horizontal dielectric slot suffers lower loss [40] compared to vertical one and higher sensitivity in bio-chemical and gas sensing applications [41–44]. The waveguide design parameters optimizations for the maximum sensitivity have been investigated by using our in-house accurate full-vectorial finite element method (FV-FEM). However, this type of HSHPW being different than standard silicon nanowire or dielectric slot guide, so we have considered the design variation to reduce the junction losses. The least squares boundary residual method (LSBR) along with the FV-FEM has also been used to obtain scattering matrices at waveguide discontinuity junctions. The MZI consists of non-identical waveguides in sensing and reference arms. The HSHPW incorporating sensing arm with isopropanol in the cover and slot regions provides a negative temperature dependent phase change, whereas the reference arm with SiO_2 clad Si/ SiO_2 /Si dielectric horizontal slot (DHS) waveguide incurs a positive temperature dependent phase change. Thus, the opposite phase changes in both arms offer a much higher cumulative phase difference for a small temperature variation. This same MZI configuration is also capable of detecting a small fractional change of isopropanol concentration in a water/isopropanol binary solution for a fixed temperature. Thus, our proposed MZI sensor not only have a high response to refractive index-based temperature sensing but also have an excellent ability to detect liquid concentration which is promising for a lab-on-chip sensor arrays. To the best of our knowledge, no such on-chip integrated photonic device has been reported which shows a single optimized device design which is highly sensitive to both temperature and refractometric changes of volume concentration of liquids.

2. Theory and design schemes

2.1 Design principle

The metal strip loaded HSHPW supports a plasmon assisted slot confined mode in the low index area which is a combination of photonic and plasmonic modes arise from dielectric-dielectric (Si/isopropanol) and dielectric-metal (isopropanol/Ag) interfaces, respectively. The 3D schematic of HSHPW structure is shown in Fig. 1(a) which contains a nano-dimension slot in between suspended Si slab and a lower Ag layer deposited on top of the SiO_2 buffer layer. The HSHPW is butt coupled to SiO_2 clad Si/ SiO_2 /Si dielectric horizontal slot (DHS) waveguides at both ends. Thus, the Si slab forms a bridge over the metal layer and offers a plasmonic slot which is exploited as a sensing region in our proposed design. Inset of Fig. 1(a) shows the cross-section view of the HSHPW. The plasmonic waveguide design, optimizations and performance analyses require an accurate mode solver to solve the partial differential equations (PDEs). In most cases, the PDEs for plasmonic problems are much complex to be solved by using conventional analytical and semi-analytical approaches. Our in-house \mathbf{H} -field based full-vectorial finite element method (FV-FEM) has been developed [45] and refined [34, 44, 46, 47] over last thirty years is used for modal solutions. The variational formulation used for FV-FEM is modified by considering local dielectric constant of each discretized element for the elimination of spurious modes, particularly useful for plasmonic waveguides [44, 47] so that their Euler equations not only follow the Helmholtz's equation but also satisfy the Maxwell's divergence equation.

$$k_0^2 = \left(\frac{\omega}{c}\right)^2 = \frac{\langle \hat{\epsilon}_r^{-1} (\nabla \times \mathbf{H}), (\nabla \times \mathbf{H}) \rangle + \langle \hat{\epsilon}_r^{-1} (\nabla \cdot \mathbf{H}), (\nabla \cdot \mathbf{H}) \rangle}{\langle \hat{\mu}_r \mathbf{H}, \mathbf{H} \rangle} \quad (1)$$

Here k_0 , ω , $\hat{\epsilon}$ and $\hat{\mu}$ denote the wavenumber, angular frequency, relative permittivity and permeability tensor, respectively and k_0^2 represents the eigenvalue. The modal phase constant (β) and effective index ($N_{eff} = n_{eff} - jk_{eff} = \beta/k_0 - j\alpha/k_0$) can be evaluated from the eigenvalues. Here α is the mode attenuation constant in **nepers per micrometer** ($Np/\mu m$) and $k_0 = 2\pi/\lambda_0$ is the plane wave phase constant in free space and λ_0 is free-space wavelength of light. An accurate solution of a plasmonic waveguide requires a sufficient dense mesh distribution around the metal film to resolve the sub-wavelength field confinement. Our flexible meshing technique associated with FV-FEM helps in this regard. The mode propagation length ($L_p = \lambda/4\pi k_{eff}$, the waveguide length where the guided mode power is $1/e$ times of its initial value) and mode power attenuation ($\alpha' (dB/\mu m) = 4.343/L_p$; $\alpha' (dB/\mu m) = 20 \cdot \log_{10} e \cdot \alpha (Np/\mu m)$) are also important in evaluation of plasmonic waveguides. Optimization to maximum waveguide sensitivity requires a rigorous assessment of power confinement factor (Γ) in the specific regions (slot and sensing regions) which can be defined as

$$\Gamma = \frac{\iint_{\Delta} Re(\mathbf{E} \times \mathbf{H}^*) \cdot \hat{z} \, dx dy}{\iint_{\infty} Re(\mathbf{E} \times \mathbf{H}^*) \cdot \hat{z} \, dx dy} \quad (2)$$

Here Δ represents the horizontal slot and/or cover medium, together with forms the sensing region. The vectorial \mathbf{E} and the complex conjugate of \mathbf{H} (\mathbf{H}^*) fields are used to formulate the modal

Poynting vector ($S_z = (\mathbf{E} \times \mathbf{H}^*) \cdot \hat{z}$). Two butt-coupling junctions of the HSHPW and DHS waveguide in the MZI sensing arm create waveguide discontinuities. The least squares boundary residual (LSBR) method [48] is used in conjugation with FV-FEM for rigorous investigations of power transfer and transmission loss of these two butt-coupled waveguides. Minimization of the vector functional $d\mathbf{G} = 0$ satisfy the continuity of the both tangential \mathbf{E} and \mathbf{H} field components on both sides of a waveguide junction and provides a stationary solution by least squares means. The functional can be represented as

$$\mathbf{G} = \int [|\mathbf{E}_t^1 - \mathbf{E}_t^2|^2 + m \cdot Z_0^2 |\mathbf{H}_t^1 - \mathbf{H}_t^2|^2] dx dy \quad (3)$$

The subscript t , superscripts numbers (1 and 2), Z_0^2 and m represents the transverse components of fields (\mathbf{E} and \mathbf{H}), the mode fields **belonging** to the right and the left side of the junction, free-space impedance and a weighting factor, respectively.

A single output, unbalanced, asymmetric arm and unequal power split/combine MZI is used as a transducer device in the detection of a small refractive index change of isopropanol depending on either temperature and volume concentration of isopropanol solution. The complete optical characterization set-up and a schematic diagram of HSHPW (in sensing arm) and DHS (in reference arm) incorporated MZI are shown in Figs. 2(a) and (b), respectively. The light from a tunable CW laser can be launched into MZI with the help of a grating coupler. The isolator can be used to prevent unwanted feedback to the CW laser cavity. The polarization controller is set-up at the input for allowing only TM mode. At the device end, an optical fiber is used to carry the characterization response to a high precision optical spectrum analyzer (OSA) for further analyses. The HSHPW is inserted in between fixed length SiO_2 clad DHS waveguides ($L_{DHS} = 10 \mu\text{m}$) on both sides (Fig. 1(a)), together they form the sensing arm of length, $L_{Sen} = 2L_{DHS} + L_{HSHPW}$. On the other hand, the reference arm of length L_{Ref} consists of only SiO_2 clad DHS with four 90° bends of radius $R_B = 5 \mu\text{m}$ (very low bending loss, thus, neglected in further calculations) and straight sections (L_{R1} , L_{R2} , and L_{R3}) to make the device feasible to change the arm length for calibration of frequency spectral range (FSR) and sensitivity (S_D). Thus, the L_{Ref} can be expressed as, $L_{Ref} = (2\pi R_B) + L_{R1} + L_{R2} + L_{R3}$. The DHS straight section, L_{R2} is considered to have same length as L_{HSHPW} in sensing arm. Therefore, only L_{R1} and L_{R3} ($L_{R1} = L_{R3}$) are left free of length calibration. The MZI has SiO_2 cladding as cover medium except for HSHPW that creates a *sensing window*, by which the liquid isopropanol is infiltrated in the sensing region (slot + cover medium). During sensing, the differential phase change ($\Delta\phi$) between both arms depends on the optical path difference (OPD) arises due to a refractive index change of isopropanol as

$$\Delta\phi = \frac{2\pi}{\lambda} [(n_{eff,DHS} \cdot 2L_{DHS} + n_{eff,HSHPW} \cdot L_{HSHPW}) - (n_{eff,DHS} \cdot L_{Ref})] \quad (4)$$

The n_{eff} with subscripts DHS and HSHPW denote the real part of the effective indices of the corresponding waveguide. Thus, for a plasmonic waveguide assisted MZI, operating at a wavelength (λ) the output power (P_{out}) depends on the OPD value through $\Delta\phi$ and that can be expressed as [49]

$$P_{out} = \frac{1}{4} \cdot P_{in} (e^{-2\alpha_{Ref}L_{Ref}} + e^{-2\alpha_{Sen}L_{Sen}}) \cdot (1 + F \cos \Delta\phi) \quad (5)$$

Here α_{Ref} , α_{Sen} represent the attenuation constants in Np/ μm associated with the reference and sensing arms waveguides, respectively and F represents the fringe visibility of MZI output given as:

$$F = \frac{2e^{-\alpha_{Ref}L_{Ref}} e^{-\alpha_{Sen}L_{Sen}}}{e^{-2\alpha_{Ref}L_{Ref}} + e^{-2\alpha_{Sen}L_{Sen}}} \quad (6)$$

It is being assumed that the input power is distributed equally (P_{in}) in both the arms. The HSHPW in the sensing arm has a significant amount of quasi-TM modal loss compared to the DHS which can be assumed to be loss-less (quasi-TM) [40] i.e. $\alpha_R = 0$ and the transmittance, $e^{-2\alpha_R L_{Ref}} = 1$ for a short length waveguide. Small scattering loss in both the branches can be included separately if necessary. The mode propagation loss in HSHPW and butt-coupling losses at the junction 1 and 2 ($J1$ and $J2$) in sensing arm (Fig. 2(b)) affect the overall device output power and its fringe visibility (F). However, it can be compensated by tuning the coupling section (L_x) of the input directional coupler so that, the sensing arm receives more power to balance the device insertion loss and thus, improve the interference fringe visibility. Furthermore, the only unaccounted loss comes from the small attenuation perturbation ($\Delta\alpha_S$) in the sensing HSHPW during homogeneous refractometric changes of isopropanol solution. Therefore, the formulation of the MZI output power (P_{out}) can be shown to be as:

$$P_{out} = \frac{1}{2} [P_{inR} + (P_{inS} \cdot \tau_{J1} \cdot \tau_{J2} \cdot e^{-2(\alpha_{HSHPW} \pm \Delta\alpha_S)L_{HSHPW}})] (1 + F' \cdot \cos \Delta\phi) \quad (7)$$

Where the modified fringe visibility (F') is given by

$$F' = \frac{2\sqrt{P_{inR} \cdot P_{inS} \cdot \tau_{J1} \cdot \tau_{J2}} \cdot e^{-(\alpha_{HSHPW} \pm \Delta\alpha_S)L_{HSHPW}}}{P_{inR} + P_{inS} \cdot \tau_{J1} \cdot \tau_{J2} \cdot e^{-2(\alpha_{HSHPW} \pm \Delta\alpha_S)L_{HSHPW}}} \quad (8)$$

The P_{inR} and P_{inS} represent the unequally distributed input power at the reference and sensing arms, respectively. The τ_{J1} and τ_{J2} denote the transmittance at the waveguide discontinuities $J1$ and $J2$, respectively and α_{HSHPW} is the quasi-TM mode attenuation constant of the HSHPW. The frequency spectral range (FSR) of the MZI is calculated by

$$FSR = \frac{\lambda^2}{[(n_{g,DHS}L_{DHS} + n_{g,HSHPW}L_{HSHPW}) - n_{g,DHS}L_{Ref}]} \quad (9)$$

where λ , $n_{g,DHS}$ and $n_{g,HSHPW}$ are the operating wavelength and group index of DHS and HSHPW, respectively. In our design, the key point is to achieve a highly sensitive temperature sensor design

to increase the differential phase change between the two arms. This is achieved by the light guiding through materials with negative and positive TOCs in sensing and reference arms, respectively. The temperature sensitivity (S_T) of the MZI device i.e. the wavelength shift ($\Delta\lambda$) of destructive fringes with respect to temperature (T) is defined as [50]

$$S_T = \frac{FSR \cdot \left[\left(\frac{dn_{eff,DHS}}{dT} \right) \cdot L_{DHS} + \left(\frac{dn_{eff,HSHPW}}{dT} \right) \cdot L_{HSHPW} \right] - \left(\frac{dn_{eff,DHS}}{dT} \right) \cdot L_{Ref}}{\lambda} \quad (10)$$

2.2 Waveguide materials

The wavelength and temperature dependent Si refractive indices are obtained from the Sellmeier equation [51], valid for the wavelength and temperature range of 1.2 to 14 μm and -173 to 476 $^\circ\text{C}$, respectively. SiO_2 has positive TOC (dn/dT) of $+1.1 \times 10^{-5} / ^\circ\text{C}$ and its refractive indices have been calculated by the Sellmeier equation [52]. Besides, the liquid isopropanol has a high negative TOC of $-4.5 \times 10^{-4} / ^\circ\text{C}$ and its refractive index as a function of wavelength is obtained from a least-squares approximation based Sellmeier equation [53] acceptable for the wavelength range of 0.185 – 2.8 μm . The temperature dependent complex refractive index of the metal (Ag) is evaluated by the Drude model [54], can be expressed as

$$\epsilon(\lambda) = \epsilon_r + j\epsilon_i = \epsilon_\infty - \frac{\omega_p^2}{\omega(\omega + j\omega_c)} \quad (11)$$

here the parametric values of ϵ_∞ and collision frequency (ω_c) for Ag are taken as 3.1 and 0.31×10^{14} rad/s. The plasma frequency (ω_p) has a strong temperature dependency and is given by, $\omega_p = \omega_{p0} \cdot e^{-A_V(T_0)(T-T_0)/2}$, where ω_{p0} , A_V are the plasma frequency at the ideal/room temperature, T_0 and volume expansion coefficient ($A_V = 3A_L = 5.7 \times 10^{-5} / ^\circ\text{C}$) of Ag, respectively.

By considering the TOC (dn/dT), the variation of isopropanol refractive index with temperature is obtained by, $n_T = n_{T_0} + (T - T_0)dn/dT$, where n_{T_0} and n_T are the refractive indices of the isopropanol at a known and desired temperature T_0 and T , respectively. Additionally, the refractive index variation of isopropanol/water solution depends on the volume concentration of isopropanol and is determined by using the Lorentz-Lorenz equation [44] for a binary solution.

3. Analyses and results

3.1 Optimization of waveguide parameters

The sensing slot in HSHPW is sandwiched between a thin metal (Ag) layer and another suspended high index Si slab bridged between two DHS waveguides at both the ends (Fig. 1). The thin Ag layer on SiO_2 buffer not only provides the sub-wavelength confinement but also restricts penetration of evanescent field into buffer region. This restricted field that **intends to expand** into the dielectric substrate for the all-dielectric slot waveguide is now guided through the low index

slot above the metal. This in turn increases the power confinement in the slot and sensing region (slot + cover medium) compared to a conventional dielectric horizontal slot waveguide. The HSHPW dimensions, such as waveguide width (W_{Si}), metal thickness (H_{Ag}), Si slab height (H_{Si}), and slot height (H_{slot}) are optimized to confine the maximum power inside the low index slot region at the operating wavelength of 1550 nm. In this case, the slot and cover medium are considered to be filled with 100% isopropanol. Throughout the FV-FEM simulations, existing one-fold symmetry is exploited and only half of the waveguide is discretized with 1,280,000 non-uniform triangular elements with a minimum element size of 0.2 nm close to the metal surface to resolve the sub-wavelength field confinement accurately. **Figures 3(a) and (b) depict E_y field distributions of the quasi-TM fundamental mode of DHS and HSHPW, respectively. The dominant E_y field is mostly confined in the low index horizontal slot region of the DHS and HSHPW. However, compared to SiO_2 clad DHS waveguide, the HSHPW confined more power in the horizontal slot region containing isopropanol, as preferred. In Fig. 3(c), the solid blue and red dashed lines depict the normalized 1D field plots of E_y (top) and H_x (bottom) fields along y-axis of HSHPW and DHS waveguide, respectively. The quasi-TM H_x field of the DHS (red dashed line) is continuous, showing its two peaks in the top and bottom Si layers and a lower value in the low index SiO_2 slot. The dominant E_y field of the similar waveguide shows a symmetric distribution along y-axis with a maximum confinement in the slot. The quasi-TM H_x field of the HSHPW shows a positive peak in the Si layer, and a small negative peak at the interface of thin Ag layer and low index slot region. On the other hand, the dominant E_y field is confined maximally in the low index isopropanol contained slot, and moderately in the top clad region (blue solid line). This E_y field is useful for the detection of a small refractometric change. Additionally, the Ag+ SiO_2 buffer layer of HSHPW only confines a very low ~0.1% of light. Therefore, the rest of the guided light is considered to enhance the slot and sensing region confinement, and also sensitivity of the waveguide.**

The variations of n_{eff} , α' (dB/ μ m), and slot confinement (Γ_{slot}) of HSHPW with H_{Ag} are shown in Fig. 4. The inset figure shows the confinement in the Ag layer (Γ_{Ag}) against H_{Ag} . Other parameters, W_{Si} , H_{Si} and H_{slot} are kept fixed at 700, 150, and 100 nm, respectively. It can be observed that for the fixed values of W_{Si} , H_{Si} , and H_{slot} , the H_{Ag} variations within the range of 80 to 1000 nm have no visible effect on n_{eff} , α' , and Γ_{slot} . But for any value of H_{Ag} lower than 80 nm, all four parameters increase rapidly. Γ_{slot} increases from its base value of 58.59% to 59% **shows a very small change. Besides**, the confinement in the lossy Ag layer (Γ_{Ag}) **shows a rapid increment** from its base value of 0.101% to a high 4.044%, which results in a larger change **in mode attenuation from** 0.037 dB/ μ m to 0.12 dB/ μ m, that may be unacceptable for some designs. With the variation of the temperature, Ag metal thickness may be expanded in the normal direction. Thus, over the complete range of temperature variation (20°C – 60°C), using the augmented thermal expansion coefficient expression $A'_L = A_L \frac{1+\mu}{1-\mu}$, shows only a 0.16% H_{Ag} increment in its thickness, where $\mu = 0.37$ is the Poisson number of Ag. Such a small thickness variation of the Ag metal film with temperature would have a negligible effect on the n_{eff} , α (Np/ μ m) and Γ_{slot} . The contour plots in Figs. 5(a) and (b) show a combined effect of W_{Si} and H_{Si} on the n_{eff} and Γ_{slot} , respectively. Here, H_{Ag} and H_{slot} are fixed at 150 and 100 nm, respectively. In this case, n_{eff} increases faster with the H_{Si} for a fixed W_{Si} than that of the W_{Si} **increases** for a fixed H_{Si} . The Γ_{slot} contour distribution shows an enhanced slot confinement of more than 50% for the W_{Si} and H_{Si}

range of 700 to 800 nm and 100 to 180 nm, respectively. An abrupt Γ_{slot} variation is observed when $W_{Si} > 800$ nm and H_{Si} is in the range of ~ 150 to 300 nm. This local change has been identified due to the occurrence of second order quasi-TE mode (more light confines in the Si slab) within a close proximity of quasi-TM fundamental mode. In this range, further investigations were carried out to identify the optimum values of these design parameters. Figure 6(a) shows the Γ_{slot} , Γ_{clad} and $\Gamma_{slot+clad}$ variations against W_{Si} when the H_{slot} and $H_{Si} = H_{Ag}$ are fixed at 100 and 150 nm, respectively. The Γ_{slot} increases with W_{Si} , reaches a maximum value of 59.24% for $W_{Si} = 740$ nm and then decreases. On the other hand, Γ_{clad} shows a linear reduction with the increase of W_{Si} . As a result, the resultant $\Gamma_{slot+clad}$ also decreases with the increase of W_{Si} . The optimum value of W_{Si} is considered to be 740 nm which gives maximum slot confinement, $\Gamma_{slot} = 59.24\%$ and corresponding $\Gamma_{slot+clad} = 82.04\%$. Similarly, these confinement variations with H_{Si} have been shown in Fig. 6(b). In this case, the Γ_{slot} increases with H_{Si} shows a maximum confinement of 59.60% at $H_{Si} = 140$ nm and then decreases. However, $H_{Si} = 140$ nm has slightly higher loss ($\alpha' = 0.038$ dB/ μ m) compared to the 150 nm ($\alpha' = 0.036$ dB/ μ m). The Γ_{clad} decreases in a hyperbolic nature and shows $\Gamma_{clad} = 22.80\%$ when $H_{Si} = 150$ nm. Therefore, with the $\Gamma_{slot+clad} = 82.04\%$, the optimum value of H_{Si} is considered to be 150 nm.

Figures 7(a) and (b) show the quasi-TM and TE power confinements (Γ_{slot} , Γ_{clad} , and $\Gamma_{slot+clad}$) with H_{slot} when W_{Si} , H_{Si} and H_{slot} are kept fixed at 740, 150 and 150 nm, respectively. Figure 7(a) shows that with the increment of H_{slot} , the Γ_{slot} of quasi-TM mode, shown by a black solid line, increases and reaches its maximum value of 59.38% at $H_{slot} = 90$ nm and then decreases gradually with further increase. The Γ_{clad} increases with the H_{slot} shown by a red dashed line and shows a 22.80% power confinement for $H_{slot} = 100$ nm. The resultant $\Gamma_{slot+clad}$, shown by a blue dashed-dotted line, shows a bell-shaped variation with its peak value of $\Gamma_{slot+clad} = 82.04\%$ for 100 nm slot height (shown by the right-hand side scale). On the other hand, the HSHPW with $H_{slot} = 90$ nm has a comparatively higher loss (0.040 dB/ μ m) than that of the 100 nm (0.036 dB/ μ m). Likely, Fig. 7(b) shows a similar variation with the H_{slot} for the fundamental quasi-TE mode. Within the complete range (40 to 150 nm) of H_{slot} , the slot and clad region confine a much lower power (Γ_{slot} and Γ_{clad}) than that of the quasi-TM mode. As a result, the sensing region shows only ~ 30 to 34% power confinement ($\Gamma_{slot+clad}$) within the range of H_{slot} . The lower power confinement in the low index slot makes the quasi-TE mode less sensitive to the small refractometric changes of liquid isopropanol.

Summarizing the above studies, we can conclude that the fundamental quasi-TM mode of HSHPW is highly sensitive to slot refractometric changes. With the optimizing design parameters, the metal strip loaded HSHPW has shown an enhanced performance in terms of the slot, sensing region power confinement ($\Gamma_{slot} = 59.24\%$, $\Gamma_{slot+clad} = 82.04\%$) and the mode power attenuation, $\alpha'_{HSHPW} = 0.036$ dB/ μ m. Finally, all the optimized HSHPW dimensions with 100% isopropanol can be summarized as, Si slab/waveguide width (W_{Si}) = 740 nm, height (H_{Si}) = 150 nm, slot height (H_{slot}) = 100 nm and the thickness of Ag strip (H_{Ag}) = 150 nm for the operating wavelength of $\lambda = 1550$ nm.

3.2 MZI design with HSHPW and DHS waveguide

The sensing arm of the MZI consists of active and optimized isopropanol filled HSHPW butt-coupled with DHS waveguides at both the ends. The waveguide discontinuities at the HSHPW-DHS junctions ($J1$ and $J2$) incur additional coupling losses along with the inherent plasmonic

mode propagation loss of the HSHPW. These waveguide discontinuities have been analyzed by using the LSBR (Eq. 3) method and the result shows the transmission coefficient at the HSHPW-DHS junction is $\rho_{J1} = \rho_{J2} = 0.85339$. Thus, the junction transmittance has the value of $\tau_{J1} = \tau_{J2} = |\rho|^2 = 0.73$ which yields the insertion loss at each junction of 1.377 dB. For the MZI design purpose, we have considered three different HSHPW lengths (L_{HSHPW}) such as 20, 30 and 40 μm . These three waveguide lengths provide the transmittance ($\tau_{HSHPW} = e^{-2\alpha_{HSHPW}L_{HSHPW}}$) values of 0.84, 0.78 and 0.71, respectively. Thus, the total transmittance values ($\tau_{Sen} = \tau_{J1} \cdot \tau_{J2} \cdot \tau_{HSHPW}$) of the HSHPW incorporated sensing arm for $L_{HSHPW} = 20, 30, \text{ and } 40 \mu\text{m}$ are 0.45, 0.41, and 0.38, respectively. An equal power division (50:50) at the reference and sensing arms of this type of plasmonic waveguide assisted MZI will result in an imbalance of light intensity at both the arms which in turn provides a poor interference fringe visibility (F) at the output (P_{out}). This shortcoming can be mitigated by using asymmetric power splitting in the sensing and reference arms. To obtain unequal power splitting, the coupling section (L_x) of the input directional coupler can be adjusted depending on the power requirements in the sensing arm, $P_{in-Sen} = 1/(1 + \tau_{Sen})$ and reference arm, $P_{in-Ref} = (1 - P_{in-Sen})$. Figure 8(a) shows a graphical representation of the P_{in-Sen} and P_{in-Ref} requirement depending on the length of HSHPW used for sensing. As the junction ($J1$ and $J2$) losses due to waveguide discontinuities are constant, so the only variable loss is considered for power fraction calculation is the modal loss due to different L_{HSHPW} . With the increment of L_{HSHPW} from 10 to 50 μm , the mode propagation loss increases from 0.36 to 1.84 dB. To counter that, the input power distribution ratio (P_{in-Sen}/P_{in-Ref}) needs to be changed from 67% / 33% to 74% / 26%. The required P_{in-Sen} and P_{in-Ref} for $L_{HSHPW} = 20, 30, \text{ and } 40 \mu\text{m}$ are 0.69, 0.71, 0.72, and 0.31, 0.29 and 0.28 respectively, shown by the red and blue lines. These unequal power distributions not only compensate for the losses in sensing arm but also improve the P_{out} with a very high interference fringe visibility ($F' \sim 1$), which is highly required for an accurate measurement. The asymmetric power distribution demands an appropriate tuning of coupling section at the input directional coupler. Figure 8(b) represents the desired coupling section (L_x) variations of SiO_2 clad DHS waveguide based directional coupler (inset of Fig. 8(b)) as a function of gap (separation) between two DHS waveguides and the L_{HSHPW} . The desired length of the coupling section (L_x) can be calculated from the original coupling length (L_c) and the P_{in-Sen} as, $L_x = (2L_c/\pi) \cdot \cos^{-1} \sqrt{P_{in-Sen}}$. The L_x value increases as the gap increases from 250 nm to 450 nm. Moreover, with the increase of L_{HSHPW} the L_x linearly decreases a constant gap. For a smaller gap, the L_x has a smaller value than for a **larger** gap. Hence, depending on the user's preferences, one can easily choose a suitable gap and the corresponding L_x values for different L_{HSHPW} . As an example, for the gaps of 350 and 400 nm, the L_x values for $L_{HSHPW} = 20, 30 \text{ and } 40 \mu\text{m}$ are 10.99, 10.64, 10.29 μm and 13.98, 13.53 and 13.09 μm , respectively, to achieve the required asymmetric power distributions.

3.3 Device performance as a sensor

A well designed MZI sensor needs a significant attention on the calibration of free spectral range (FSR) and interference fringe visibility (F') of the output power, P_{out} . After setting up the optimized waveguide design parameters for the MZI arms, L_{HSHPW} and L_x for the input directional coupler, the FSR and F' parameters are investigated and evaluated as a function of L_{Ref} and L_{HSHPW} , respectively. The fringe visibility will have the maximum value ($F = F' = 1$) when the two MZI light beams have equal intensity. Inherent modal and junctional losses drop the sensing

arm light output thus degrade the interference fringe visibility. With the unequal power distributions, more power is launched at the sensing arm input which not only balance the losses but also provides an equal output at both MZI arms. Figure 9(a) depicts the advantages of using an unequal power distribution over the more traditional 50:50 power splitting. The black line indicates a significant reduction of the F parameter with the increase of L_{HSHPW} . However, the unequal power splitting shows a significant improvement with almost an ideal value of $F' \approx 1$. Under this condition, the F' parameters are calculated with the augmented visibility equation (Eq. 7) and the results show a very high fringe visibility ($F' \approx 1$) for all L_{HSHPW} s in expenses with increasing insertion loss. For these three L_{HSHPW} s (20, 30 and 40 μm) incorporating unequal power splitting the device insertion losses are 2.06, 2.32 and 2.56 dB, respectively when 100% isopropanol is used at temperature $T = 20$ °C. Beside the visibility, the FSR is another important parameter which indicates the frequency spacing of the MZI transmission peaks. A unit wavelength changes with very small power change results in a large FSR which may be unacceptable due to added difficulties in detection of the interference wavelength by optical spectrum analyzer (OSA). Thus, as a compromise, a relatively small FSR values of 10 and 15 nm have been considered and the arm lengths are calibrated accordingly. The FSR is calculated as a function of L_{Ref} and L_{Sen} (Eq. 8) and the results are shown in Fig. 9(b). The variations indicate that the lower FSR requires higher L_{Ref} for a fixed L_{HSHPW} . The horizontal black dashed lines indicate the 10 and 15 nm FSR and its corresponding L_{Ref} values for a fixed L_{HSHPW} . In our design, the L_{Ref} calibration only demands the change in the straight waveguide sections (L_{R1} , L_{R2} and L_{R3}) as the bending sections of radius 5 μm cover a fixed length of $L_B = 31.42$ μm . For the three fixed L_{HSHPW} values (20, 30 and 40 μm) the reference arm length ($L_{Ref} = 2\pi R_B + L_{R1} + L_{R2} + L_{R3}$) with different sections to obtain FSR = 10 and 15 nm are tabulated in Table 1.

Our aim is to design the MZI for the temperature and the volume concentration sensing of any liquid. In this study, we have considered liquid isopropanol for our investigations. The quasi-TM effective index difference (TM- Δn_{eff}) of the optimized HSHPW and the DHS waveguide with the temperature for 100% isopropanol are shown in Fig. 10(a). The red line shows a positive and linear Δn_{eff} variation of SiO_2 clad DHS waveguide, whereas, the blue dashed line shows the same Δn_{eff} variation of the HSHPW but in the negative direction. The positive and negative TM- Δn_{eff} variations of the HSHPW and the DHS provides a temperature dependent opposite phase change in both arms which enhance the temperature sensitivity of the device. The quasi-TM effective index variation with temperature (dn_{eff}/dT) of both the HSHPW and DHS are $-4.61 \times 10^{-4}/^\circ\text{C}$ and $+6.62 \times 10^{-5}/^\circ\text{C}$, respectively. The black line in Fig. 9(b) represent a negative quasi-TM Δn_{eff} variation of the optimized HSHPW with the volume fraction of isopropanol in the isopropanol/water solution at a fixed temperature, $T = 20$ °C. During volume concentration sensing, the temperature is kept fixed so that the only refractive index change occurs at the HSHPW due to the different concentration of isopropanol in the solution. The refractometric sensitivity of the HSHPW can be evaluated as, $S_{HSHPW} = \Delta n_{eff}/\Delta n = 1.13$. The HSHPW shows a higher refractive index sensitivity compared to a recently published complex hollow hybrid plasmonic design scheme [39].

Figures 11(a), (b), and (c) on the left side show the transmitted P_{out} spectra for the proposed MZI temperature sensor with $L_{HSHPW} = 20, 30,$ and 40 μm , respectively for 10 nm FSR. Whereas, the figures in the right columns (Figs. 11(d), (e), and (f)) depict the MZI responses for the same three L_{HSHPW} values, but for 15 nm FSR. Different colored curves signify different temperatures

(varied from 20°C to 60°C) of 100% isopropanol infiltrated in the sensing HSHPW region. It can be clearly observed that with the temperature increment the MZI transmission spectra show the red shift (towards the right) because of a larger TOC of isopropanol compared to other materials such as Si, Ag, and SiO_2 . It should be noted that the wavelength shifts ($\Delta\lambda_T$) increase with the increment of L_{HSHPW} and FSR. A temperature variation from 20°C to 60°C for the MZI design with $L_{HSHPW} = 20, 30,$ and $40 \mu\text{m}$ shows the $\Delta\lambda_T$ of 4.25, 5.66, and 6.87 nm red shift, respectively, for FSR = 10 nm. Similarly, for the same temperature variations with aforementioned L_{HSHPW} lengths the output transmission spectra are red shifted more by 5.48, 7.43, and 9.76 nm for FSR = 15 nm. Device insertion losses for 20, 30, and $40 \mu\text{m}$ long HSHPW have the values around 2.06, 2.32, and 2.58 dB, respectively and the corresponding extinction ratios are larger than 25 dB. Figures 11(g) and (h) illustrate a linear increasing relationship of $\Delta\lambda_T$ with the temperature (T) with 100% isopropanol concentration for 10 and 15 nm FSR, respectively. For the temperature ranging from 20°C - 60°C, the $\Delta\lambda_T$ increases linearly with the increment of the T for all MZI designs with $L_{HSHPW} = 20, 30,$ and $40 \mu\text{m}$ are shown by black, red, and blue lines, respectively. Changes for FSR = 10 nm are shown in Fig. 11(g) and for FSR = 15 nm in Fig. 11(h) by dashed and dashed-dotted lines, respectively. The device sensitivities (S_T) can be evaluated from the slope of the fitted curves with the R^2 value of 0.999. Thus, for the MZI with $L_{HSHPW} = 20, 30,$ and $40 \mu\text{m}$ has the temperature sensitivity (S_T) values of 105.2 pm/°C, 140.6 pm/°C, and 172 pm/°C for FSR = 10 nm, respectively and 138.1 pm/°C, 187 pm/°C, and 243.9 pm/°C, respectively for FSR = 15 nm which indicate much higher values compared to the recent published reports [27, 28]. Additionally, our proposed design works well in a wide temperature range from room temperature (~20°C) to the boiling point of isopropanol (82°C). **Even other liquid chemicals with high boiling point could be used for temperature detection.** Moreover, the sensing range (FSR/S_T) of the designed device with $L_{HSHPW} = 40 \mu\text{m}$ can be derived for 10 and 15 nm FSR as ~58°C and ~61°C, respectively. Detection limit (DL_T) is another important characteristic of a sensor that illustrate the efficiency to resolve a smallest refractometric change of the target and it can be defined as the ratio of resolution of the transmission spectra (λ_{Res}) to the device sensitivity (S_T). The λ_{Res} of a device depends not only on the resolution of the source and the measurement equipment (OSA) but also influenced by the extinction of the device and the noise present on the measured spectra. Thus, instead of using a specific λ_{Res} value for a laser source and OSA, we have considered the device λ_{Res} as 1 pm (approx.) for our theoretical investigations and as a result, our design with $40 \mu\text{m}$ HSHPW can have the temperature detection limit or resolution (DL_T) of 0.0058°C and 0.004°C for the 10 and 15 nm FSR, respectively.

Next, the feasibility of the same MZI sensor for the detection of volume concentration of isopropanol in the isopropanol/water solution at a constant temperature is also studied. For this study, we kept the temperature fixed at 20°C. Figures 12 (a) – (c) show the MZI transmission responses of the 20, 30, and $40 \mu\text{m}$ long HSHPW as a refractometric sensor with the FSR value of 10 nm and Figs. 12 (d), (e), and (f) for FSR = 15 nm. The black spectrum represents the transmission output for 100% isopropanol at T = 20°C. Different colored spectra indicate different volume fraction of isopropanol and they also show a red shift of the wavelength ($\Delta\lambda_C$) with the isopropanol volume concentration. These wavelength shifts ($\Delta\lambda_C$) increase with the increment of both the L_{HSHPW} and FSR. The extinction ratios for the device have the values larger than 20 dB and the insertion losses were almost **similar to** those calculated with 100% isopropanol at T = 20°C. These $\Delta\lambda_C$ s with the refractometric changes of the isopropanol solution are plotted in the **Figs. 12(g) and (h)** for 10 and 15 nm FSR values, respectively. It can be observed that the $\Delta\lambda_C$

linearly increases with the reduction of isopropanol volume concentration. The horizontal x-axis indicates the refractive indices of isopropanol/water solution depending on the volume concentration (100% to 0%) of isopropanol. Therefore, the concentration sensitivities (S_C) are determined from the slope of the linearly fitted curves with $R^2 = 0.999$. Thus, for the detection of isopropanol volume concentration, the sensitivity (S_C) of the designed MZI with $L_{HSHPW} = 20, 30$ and $40 \mu\text{m}$ reaches 144.6 nm/RIU, 222.2 nm/RIU, and 290.3 nm/RIU, respectively for FSR = 10 nm and 218.1 nm/RIU, 327.6 nm/RIU, and 437.3 nm/RIU, respectively for FSR = 15 nm. It can be noted that the sensitivity increases linearly with the FSR and sensor length, L_{HSHPW} . For the same device wavelength resolution ($\lambda_{Res} = 1 \text{ pm}$), our MZI sensor with $40 \mu\text{m}$ long HSHPW shows a considerable potential to measure the refractometric changes as small as 3.44×10^{-6} and 2.28×10^{-6} RIU for the 10 and 15 nm FSR, respectively. These results show an improved refractometric sensitivity compared to the hybrid plasmonic MZI design reported recently [39].

The HSHPW incorporated MZI device can also be used for surface sensing applications. We considered an ultra-thin biolayer of different thickness ($t_{bio} = 5, 10, \text{ and } 15 \text{ nm}$) having refractive index of 1.45 [34] on both the Si slab and slot region. The cover medium and the slot is filled with water solution. Figures 13(a) and (b) show the MZI output power spectra (P_{out}) with $L_{HSHPW} = 40 \mu\text{m}$ for the FSR values of 10 and 15 nm, respectively. The black curve represents the output spectrum for $t_{bio} = 0 \text{ nm}$. Different colored spectra for different biolayer thickness ($t_{bio} = 5, 10, \text{ and } 15 \text{ nm}$) show blue shifts. These wavelength shifts ($\Delta\lambda_{bio}$) for two different FSR values (10 and 15 nm) are plotted against biolayer thickness (t_{bio}) in Fig. 13(c), shown by the blue dashed and red dashed-dotted lines. The $\Delta\lambda_{bio}$ shows a linear decrement with t_{bio} for both the FSR values. The MZI sensitivities (S_{bio}) for the detection of surface binding biomolecules are evaluated from the slope of the linear fitted curves with $R^2 = 0.999$. The surface sensitivity (S_{bio}) of the device for the FSR values of 10 and 15 nm are -605.10 pm/nm and -920.30 pm/nm, respectively. It is also worth to notice that the extinction ratio of the proposed during surface sensing is larger than -25 dB.

4. Conclusion

In conclusion, we report here the design of a novel metal strip loaded HSHPW which with its optimized designed parameters shows an enhanced power confinement of 59.24% and 82.04% in the low-index slot and possible total sensing region along with a low and acceptable loss. By integrating this HSHPW with the SiO_2 clad DHS waveguide results in a compact on-chip MZI sensing system, which not only shows a high sensitivity to the liquid temperature but also have a great potential in the detection of the liquid concentration. Waveguide optimizations, junction analyses and device performance have been studied theoretically with our in-house accurate FV-FEM and the LSBR methods. Our optimized HSHPW design shows a much higher refractometric sensitivity of 1.13. The MZI temperature sensitivity (S_T) are 105.2 pm/°C and 138.1 pm/°C for $20 \mu\text{m}$ long HSHPW in the sensing arm for the FSR values of 10 and 15 nm, respectively, and it can be increased to 172 pm/°C and 243.9 pm/°C with the $40 \mu\text{m}$ L_{HSHPW} . The same device is also sensitive to the changes of liquid volume concentrations. The device sensitivity (S_C) for concentration detection shows a high value of 144.6 nm/RIU and 218.1 nm/RIU for the $20 \mu\text{m}$ HSHPW and it shows a great enhancement to 290.3 nm/RIU and 437.3 nm/RIU for the higher value of HSHPW length ($40 \mu\text{m}$). Additionally, the proposed MZI sensor is also suitable for the detection of binding biomolecules in the sensing region. The MZI design with $L_{HSHPW} = 40 \mu\text{m}$

exhibits the surface sensitivities of -605.10 pm/nm and -920.30 pm/nm for the FSR values of 10 and 15 nm, respectively. The effect of HSHPW modal loss and the junction losses are mitigated by using unequal power splitting at the MZI input which results in very high interference fringe visibility i.e. $F' \approx 1$. The low insertion loss, high fringe visibility, high extinction ratio, and most importantly enhanced sensitivities make the design attractive for bio-sensing and chemical analyses. On the other hand, the waveguide materials such as Si, SiO_2 , and noble metal (Ag) have high melting points and also nonreactive to biofluids, oils, and common liquid chemicals. Therefore, a broad range of liquids with enough high temperature could be tested by the HSHPW incorporated MZI sensor. Thus, our proposal serves the successful demonstration of an on-chip compact MZI sensor that can be realized with the help of well-matured state-of-the-art CMOS fabrication technologies. Both temperature and concentration sensors can be integrated in an on-chip arrayed design for simultaneous detection of both. Based on the preliminary results, this MZI sensor shows a great potential to be employed as a refractometric based temperature, liquid concentration, and surface sensing device.

Acknowledgements

This work was supported by City, University of London and in part by Erasmus Mundus AREAS+ PhD fellowship and SPIE Optics and Photonics Education Scholarship 2017 program for PhD and research funding.

References

- [1] R. F. Oulton, V. J. Sorger, D. A. Genov, D. F. P. Pile, & X. Zhang, A hybrid plasmonic waveguide for subwavelength confinement and long-range propagation, *Nature Photonics* 2 (2008) 496
- [2] D. Dai and S. He, A silicon-based hybrid plasmonic waveguide with a metal cap for a nano-scale light confinement, *Opt. express* 17 (2009) 16646 – 16653
- [3] P. D. Flammer, J. M. Banks, T. E. Furtak, C. G. Durfee, R. E. Hollingsworth, and R. T. Collins, Hybrid plasmon/dielectric waveguide for integrated silicon-on-insulator optical elements, *Opt. express* 18 (2010) 21013 – 21023
- [4] H. S. Chu, E. P. Li, P. Bai, and R. Hegde, Optical performance of single-mode hybrid dielectric-loaded plasmonic waveguide-based components, *Appl. Phys. Lett.* 96 (2010) 221103-1 – 3
- [5] V. M. N. Passaro, C. de Tullio, B. Troia, M. L. Notte, G. Giannoccaro, and F. De Leonardis, Recent advances in integrated photonic sensors, *Sens.* 12 (2012) 15558 – 15598
- [6] V. M. N. Passaro, M. La Notte, B. Troia, L. Passaquindici, F. De Leonardis, G. Giannoccaro, Photonic structures based on slot waveguides for nanosensors: state of the art and future developments, *Int. J. Rev. Appl. Sci.* 11 (2012) 8 – 26
- [7] J. Homola, S. S. Yee, G. Gauglitz, Surface plasmon resonance sensors: review, *Sens. and Actuators B Chem.* 54 (1999) 3 – 15

- [8] J. Homola, Present and future of surface plasmon resonance biosensors, *Anal. Bioanal. Chem.* 377 (2003) 528 – 539
- [9] S. C. Tan, and B. C. Yiap, DNA, RNA, and protein extraction: the past and the present, *J. Biomed. Biotechnol.* 2009 (2009) 1 – 10
- [10] H. Chen, M. Rangasamy, S. Y. Tan, H. Wang, B. D. Seigfried, Evaluation of five methods for total DNA extraction from western corn rootworm beetles, *PLoS ONE* 5 (2010) 1 – 6
- [11] H. Chen, M. Ramachandra, and R. Padmanabhan, Biochemical characterization of a temperature-sensitive adenovirus DNA polymerase, *Virology* 205 (1994) 364 – 370
- [12] N. Hirayama and Y. Sano, Fiber Bragg grating temperature sensor for practical use, *ISA Trans.* 39 (2000) 169 – 173
- [13] Y. J. Rao, D. J. Webb, D. A. Jackson, L. Zhang, and I. Bennion, In-fiber Bragg grating temperature sensor system for medical applications, *J. Lightwave Technol.* 15 (1997) 779 – 784
- [14] M. Sun, B. Xu, X. Dong, and Y. Li, Optical fiber strain and temperature sensor based on an in-line Mach-Zehnder interferometer using thin core fiber, *Opt. Commun.* 285 (2012) 3721 – 3725
- [15] S. J. Qiu, Y. Chen, F. Xu, and Y. Q. Lu, Temperature sensor based on an isopropanol-sealed photonic crystal fiber in-line interferometer with enhanced refractive index sensitivity, *Opt. Lett.* 37 (2012) 863 – 865
- [16] Q. Sun, X. Sun, W. Jia, Z. Xu, H. Luo, D. Liu, and L. Zhang, Graphene-assisted microfiber for optical-power based temperature sensor, *IEEE Photonics Technol. Lett.* 28 (2016) 383 – 386
- [17] Z. Zhu, L. Liu, Z. Liu, Y. Zhang, and Y. Zhang, Surface-plasmon-resonance-based optical-fiber temperature sensor with high sensitivity and high figure of merit, *Opt. Lett.* 42 (2017) 2948 – 2951
- [18] S. Weng, L. Pei, J. Wang, T. Ning, and J. Li, High sensitivity D-shaped hole fiber temperature sensor based on surface plasmon resonance with liquid filling, *Photon. Res.* 5 (2017) 103 – 107
- [19] M. Deng, L. Liu, Y. Zhao, G. Yin, and T. Zhu, Highly sensitive temperature sensor based on an ultra-compact Mach-Zehnder interferometer with side-opened channels, *Opt. Lett.* 42 (2017) 3549 – 3552
- [20] G. -D. Kim, H.-S. Lee, C. H. Park, S. S. Lee, B. T. Lim, H. K. Bae, and W. G. Lee, Silicon photonic temperature sensor employing a ring resonator manufactured using a standard CMOS process, *Opt. Express* 18 (2010) 22215 – 22221
- [21] N. N. Klimov, M. Berger, and Z. Ahmed, Towards reproducible ring resonator based temperature sensors, *Sens. Transducers* 191 (2015) 63 – 66

- [22] N. N. Klimov, T. Purdy, and Z. Ahmed, Fabry-Perot cavity-based silicon photonic thermometers with ultra-small footprint and high sensitivity, in *Advanced Photonics 2015*, OSA Technical Digest, paper SeT4C.4.
- [23] C. M. Chang, and O. Solgaard, Fano resonances in integrated silicon Bragg reflectors for sensing applications, *Opt. Express* 21 (2013) 27209 – 27218
- [24] N. N. Klimov, S. Mittal, M. Berger, and Z. Ahmed, On-chip silicon waveguide Bragg grating photonic temperature sensor, *Opt. Lett.* 40 (2015) 3934 – 3936
- [25] A. Irace, and G. Breglio, All-silicon optical temperature sensor based on Multi-Mode Interference, *Opt. Express* 11 (2003) 2807 – 28112
- [26] J. F. Tao, H. Cai, Y. D. Gu, J. Wu, and A. Q. Liu, Demonstration of a photonic-based linear temperature sensor, *IEEE Photonics Technol. Lett.* 27 (2015) 249 – 271
- [27] X. Guan, X. Wang, and L. H. Frandsen, Optical temperature sensor with enhanced sensitivity by employing hybrid waveguides in a silicon Mach-Zehnder interferometer, *Opt. Express* 24 (2016) 16349 – 16356
- [28] Y. Zhang, P. Liu, S. Zhang, W. Liu, J. Chen, and Y. Shi, High sensitivity temperature sensor based on cascaded silicon photonic crystal nanobeam cavities, *Opt. Express* 24 (2016) 23037 – 23043
- [29] Q. Liu, X. Tu, W. Kim, J. S. Kee, Y. Shin, K. Han, Y.-J. Yoon, G.-Q. Lo, and M. K. Park, Highly sensitive Mach-Zehnder interferometer biosensor based on silicon nitride slot waveguide, *Sens. and Actuators B Chem.* 188 (2013) 681 – 688
- [30] S. Y. Nam, H. J. Chun, and Y. Mo Lee, Pervaporation separation of water-isopropanol mixture using carboxymethylated poly(vinyl alcohol) composite membranes, *J. Appl. Polym. Sci.* 72 (1999) 241 – 249
- [31] X. Wang, X. Guan, Q. Huang, J. Zheng, Y. Shi, and D. Dai, Suspended ultra-small disk resonator on silicon for optical sensing, *Opt. Lett.* 38 (2013) 5405 – 5408
- [32] T. Claes, J. G. Molera, K. D. Vos, E. Schacht, R. Baets, and P. Bienstman, Label-free biosensing with a slot-waveguide based ring resonator in silicon-on-insulator, *IEEE Photon. J.* 1 (2009) 197 – 204
- [33] S. Chandran, R. K. Gupta, and B. K. Das, Dispersion enhanced critically coupled ring resonator for wide range refractive index sensing, *IEEE J. Sel. Top. Quantum Electron.* 23 (2017) 82000109 – 1 – 8200109 – 9
- [34] S. Ghosh, and B. M. A. Rahman, An innovative straight resonator incorporating a vertical slot as an efficient bio-chemical sensor, *IEEE J. Sel. Top. Quantum Electron.* 23 (2017) 5200108 – 1 – 5200108 – 8
- [35] M. F. O. Hameed, A. S. Saadeldin, E. M. A. Elkaramany, and S. S. A. Obayya, Label-free highly sensitive hybrid plasmonic biosensor for the detection of DNA hybridization, *J. Lightwave Technol.* 35 (2017) 4851 – 4858

- [36] J. Flueckiger, S. Schmidt, V. Donzella, A. Sherwali, D. M. Ratner, L. Chrostowski, and K. C. Cheung, Sub-wavelength grating for enhanced ring resonator biosensor, *Opt. Express* 24 (2016) 15672 – 15686
- [37] X. Sun, D. Dai, L. Thylen, and L. Wosinski, High-sensitivity liquid refractive-index sensor based on Mach-Zehnder interferometer with a double-slot hybrid plasmonic waveguide, *Opt. Express* 23 (2015) 25688 – 25699
- [38] **M. S. Kwon, Theoretical investigation of an interferometer-type plasmonic biosensor using a metal-insulator-silicon waveguide, *Plasmonics* 5 (2010) 347 – 354**
- [39] X. Sun, L. Thylen, and L. Wosinski, Hollow hybrid plasmonic Mach-Zehnder sensor, *Opt. Lett.* 42 (2017) 807 – 810
- [40] R. Sun, P. Dong, N. Feng, C. Hong, J. Michel, M. Lipson, and L. Kimerling, Horizontal single and multiple slot waveguides: optical transmission at $\lambda = 1550$ nm, *Opt. Express* 15 (2007) 17967 – 17972
- [41] S. Ghosh and B. M. A. Rahman, Full vectorial finite element modelling: a composite plasmonic horizontal slot waveguide as a bio-sensor, in: 13th International Conference on Fiber Optics and Photonics, Tech. Digest OSA, 2016, paper Tu5C.3
- [42] B. Kumari, a. Barh, R. K. Varshney, and B. P. Pal, Silicon-on-nitride slot waveguide: a promising platform as mid-IR trace gas sensor, *Sens. and Actuators B Chem.* 236 (2016) 759 – 764
- [43] B. Kumari, R. K. Varshney, and B. P. Pal, Design of chip scale silicon rib slot waveguide for sub-ppm detection of N₂O gas at mid-IR band, *Sens. and Actuators B Chem.* 255 (2017) 3409 – 3416
- [44] S. Ghosh and B. M. A. Rahman, A compact Mach-Zehnder interferometer using composite plasmonic waveguide for ethanol vapor sensing, *J. Lightwave Technol.* 35 (2017) 3003 – 3011
- [45] B. M. A. Rahman and J. B. Davies, Finite-element solution of integrated optical devices, *J. Lightwave Technol.* 2 (1984) 682 – 688
- [46] B. M. A. Rahman and J. B. Davies, Penalty-function improvement of waveguide solution by finite element, *IEEE Trans. Microwave Theory Tech.* 32 (1984) 922 – 928
- [47] S. Ghosh and B. M. A. Rahman, Evolution of plasmonic modes in a metal nano-wire studied by a modified finite element method, *J. Lightwave Technol.* 36 (2018) 809 – 818
- [48] B. M. A. Rahman, and J. B. Davies, Analysis of optical waveguide discontinuities, *J. Lightwave Technol.* 6 (1988) 52 – 57
- [49] P. Berini, Bulk and surface sensitivities of surface plasmon waveguides, *New. J. Phys.* 10 (2008) 105010 – 1- 105010 – 37
- [50] S. Dwivedi, H. D’heer, and W. Bogaerts, A compact all-silicon temperature insensitive filter for WDM and bio-sensing applications, *IEEE Photon. Technol. Lett.* 25 (2013) 2167 – 2170

- [51] H. H. Li, Refractive index of silicon and germanium and its wavelength and temperature derivatives, *J. Phys. Chem. Ref. Data* 9 (1980) 561 – 658
- [52] I. H. Malitson, Interspecimen comparison of the refractive index of fused silica, *J. Opt. Soc. Am.* 55 (1965) 1205 – 1208
- [53] E. Sani and A. Dell’Oro, Spectral optical constants of ethanol and isopropanol from ultraviolet to far infrared, *Opt. Mater.* 60 (2016) 137 – 141
- [54] C. Bohren and D. Huffman, *Absorption and Scattering of Light by Small Particle*, Wiley, 1983, Chap. 9

Figure captions

Fig. 1 3D schematic of metal (Ag) strip loaded horizontal slot hybrid plasmonic waveguide (HSHPW) butt-coupled with SiO_2 clad horizontal slot waveguide (DHS) at both ends. Inset shows the cross-section of the HSHPW which works as an active sensing region. The red dashed lines indicate the waveguide discontinuities at the HSHPW and DHS waveguide junctions.

Fig. 2 Optical characterization set-up (a) and schematic top view (b) of the metal strip loaded HSHPW incorporated asymmetric MZI. The HSHPW is butt-coupled with SiO_2 clad dielectric horizontal slot (DHS) waveguide at both ends in the sensing arm of length, $L_{Ref} = 2L_{DHS} + L_{HSHPW}$. Only DHS is employed in the reference arm having four bending sections of radius, $R_B = 5 \mu\text{m}$ and three straight sections, L_{R1} , L_{R2} , and L_{R3} . Thus, total length of the reference arm is $L_{Ref} = 2\pi R_B + L_{R1} + L_{R2} + L_{R3}$.

Fig. 3 (a) and (b) depict FV-FEM simulated E_y field distributions of the quasi-TM fundamental mode of SiO_2 clad DHS waveguide and HSHPW, respectively. Distribution of left-sided colour bars exhibit higher slot power confinement in HSHPW (b) compared to DHS waveguide (a). Blue solid and red dashed lines in top and bottom figure of (c) represent line plots of dominant E_y and H_x fields, respectively along y-axis for both waveguides. Maximum E_y field confines in the slot region and the peaks of H_x field distributions show the position of metal and high index dielectric materials in DHS and HSHPW.

Fig. 4 Effective index (n_{eff}), mode power attenuation (α'), and slot confinement (Γ_{slot}) variations with thickness (H_{Ag}) of silver metal film deposited on top of SiO_2 buffer layer. The inset figure shows the power confinement (Γ_{Ag}) variation of the Ag layer against H_{Ag} . Other parameters such as, Si slab width (W_{Si}), height (H_{Si}), and slot height (H_{slot}) are kept fixed at 700, 150, and 100 nm, respectively.

Fig. 5 The 2D contour plots in (a) and (b) show the variations of n_{eff} and Γ_{slot} , respectively as a function of W_{Si} and H_{slot} . The H_{slot} and H_{Ag} are kept fixed at 100 and 150 nm, respectively. A noticeable abrupt Γ_{slot} variation occurred when $W_{Si} > 800$ nm and H_{Si} is within ~ 150 to 300 nm.

Fig. 6 Variations of power confinement in slot (Γ_{slot}), clad (Γ_{clad}), and sensing region ($\Gamma_{slot+clad}$) with W_{Si} and H_{Si} are shown in (a) and (b), respectively. The solid black, red

dashed, and blue dashed-dotted curves represent the Γ_{slot} , Γ_{clad} , and $\Gamma_{slot+clad}$ variations, respectively. W_{Si} , H_{slot} , and H_{Si} are kept fixed at 740, 100, and 150 nm, respectively.

Fig. 7 (a) and (b) show the power confinement variations in the horizontal slot, clad, and sensing region (slot + clad) of the quasi-TM and TE modes, respectively against slot height (H_{slot}). Other parameters such as W_{Si} , H_{Si} , and H_{Ag} are kept fixed at 740, 150, and 150 nm, respectively.

Fig. 8 (a) depicts the input power requirements in the sensing and the reference arms depending on the HSHPW length in the MZI sensing arm. (b) shows desired coupling section (L_x) variations of the input directional coupler as a function of HSHPW length and gap.

Fig. 9 (a) shows the fringe visibility (F and F') of the MZI interference output with equal and unequal power splitting schemes. For the 50:50 equal and unequal power splitting, the fringe visibility parameters are calculated using Eqs. 6 and 8, respectively. (b) illustrates FSR variations as a function of reference arm length (L_{Ref}) for fixed L_{HSHPWS} .

Fig. 10 (a) Blue dashed and red solid lines represent the variation of quasi-TM effective index change ($TM-\Delta n_{eff}$) of HSHPW and DHS waveguides, respectively with the surrounding temperature. **Positive and negative linear variations with slopes $+6.62 \times 10^{-5}/^\circ\text{C}$ and $-4.61 \times 10^{-4}/^\circ\text{C}$ are obtained for DHS and HSHPW, respectively.** (b) depicts a negative linear $TM-\Delta n_{eff}$ variation of the HSHPW with isopropanol volume concentration for a fixed temperature (20°C). The slope of the curve gives the waveguide refractive index sensitivity of 1.13.

Fig. 11 (a) – (f) MZI transmitted output responses for the temperature sensing of 100% liquid isopropanol. Figures (a), (b), and (c) on the left column indicate the transmission spectra with an FSR value of 10 nm. The right-sided figures (d), (e), and (f) indicate the same with an FSR value of 15 nm. Figures in each row (a, d), (b, e), and (c, f) depict the MZI output responses for 20, 30, and 40 μm long HSHPW, respectively. (g) and (h) represent the wavelength shift ($\Delta\lambda_T$) variations with the changing temperature of isopropanol for 10 and 15 nm FSR values, respectively. Slope of each linear curve represents MZI sensitivity (S_T) as a temperature sensor.

Fig. 12 (a) – (f) indicate the MZI transmitted spectra for the volume concentration sensing of isopropanol-water solution at a fixed temperature of 20°C . The figures (a), (b), and (c) on the left column indicate the output transmission spectra with an FSR value of 10 nm. The right-sided figures (d), (e), and (f) indicate the same with an FSR value of 15 nm. Figures in each

row (a, d), (b, e) and (c, f) depict the output responses of the MZI with $L_{HSHPW} = 20, 30,$ and $40 \mu\text{m}$, respectively. (g) and (h) represent the linear variations of wavelength shift ($\Delta\lambda_C$) with the volume concentration of isopropanol for 10 and 15 nm FSR values, respectively. Slope of each linear curve represents the MZI sensitivity (S_C) as a chemical concentration sensor.

Fig. 13 Surface sensing by asymmetric MZI sensor. (a) and (b) show the MZI transmitted output power spectra for the FSR values of 10 and 15 nm, respectively for $L_{HSHPW} = 40 \mu\text{m}$. 5, 10, and 15 nm ultra-thin biolayers having refractive index of 1.45 are considered for surface sensing. (c) represents linear variations of wavelength shift ($\Delta\lambda_{bio}$) against biolayer thickness (t_{bio}). Slope of each linear curve denotes device sensitivity (S_{bio}) to detect binding of biomolecules at the sensing region.

Figures

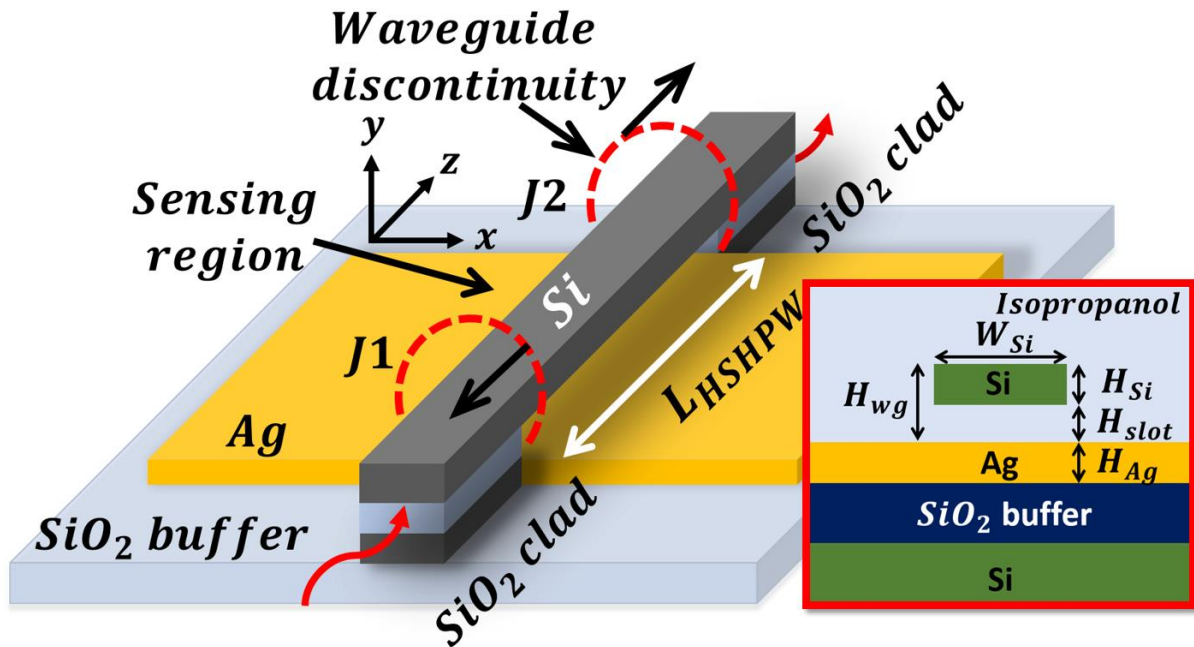


Fig. 1

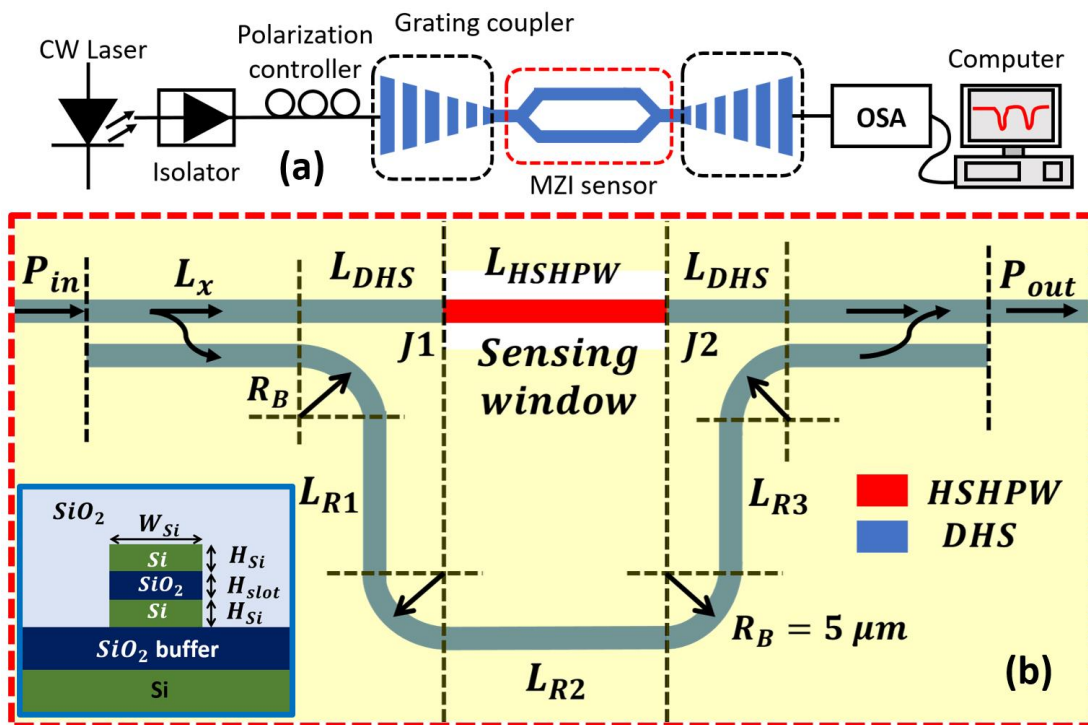


Fig. 2

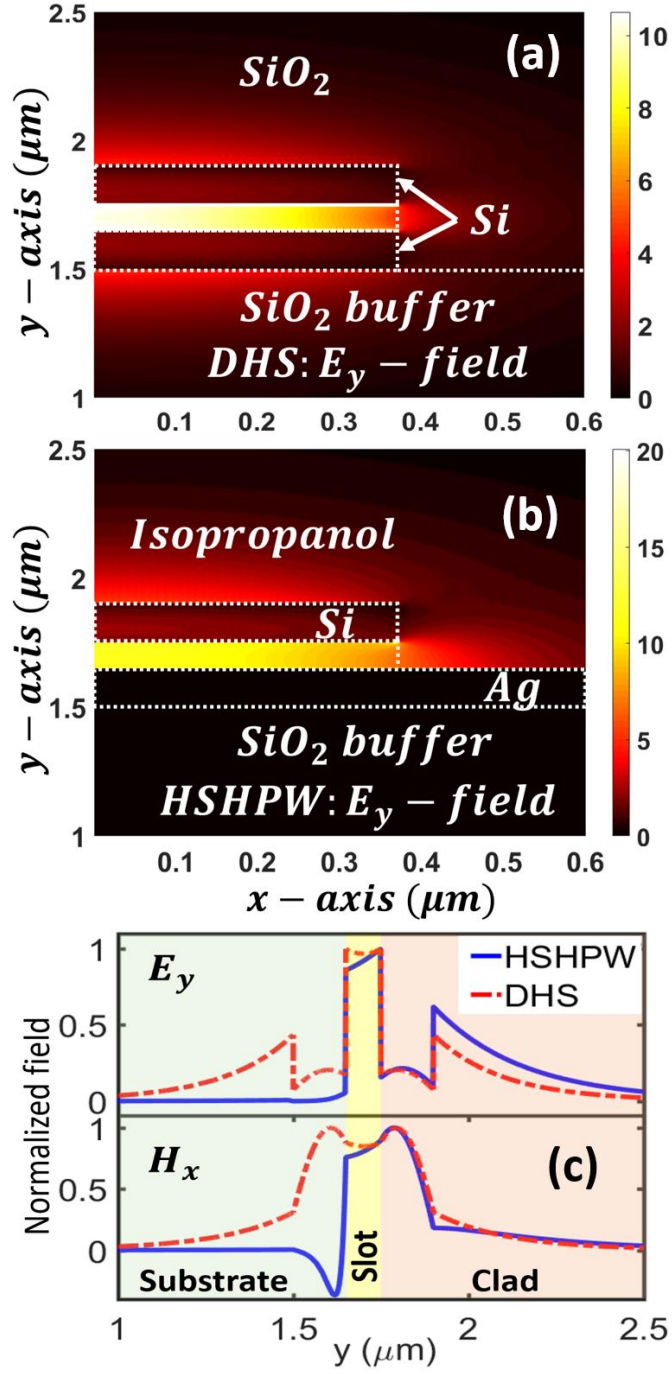


Fig. 3

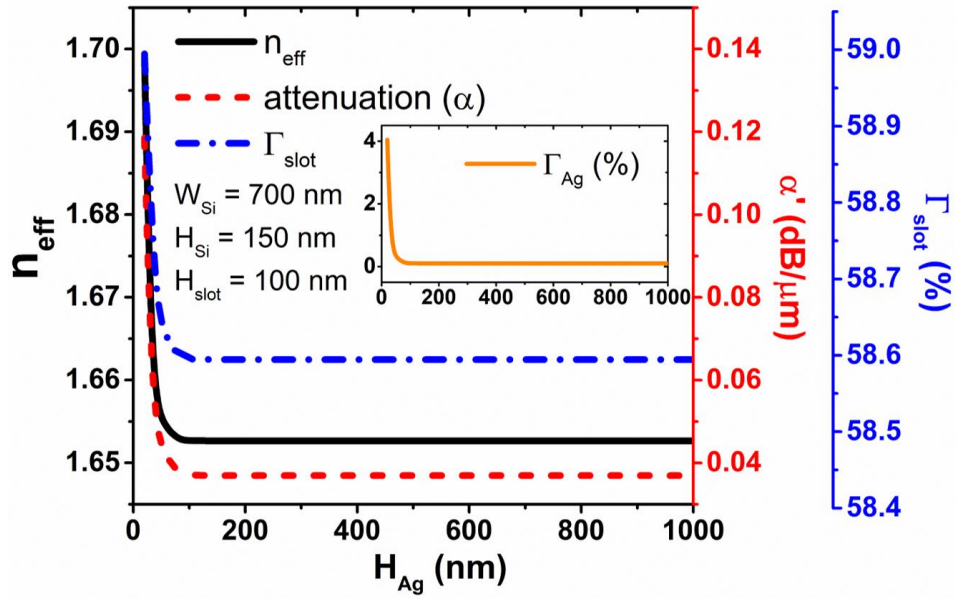


Fig. 4

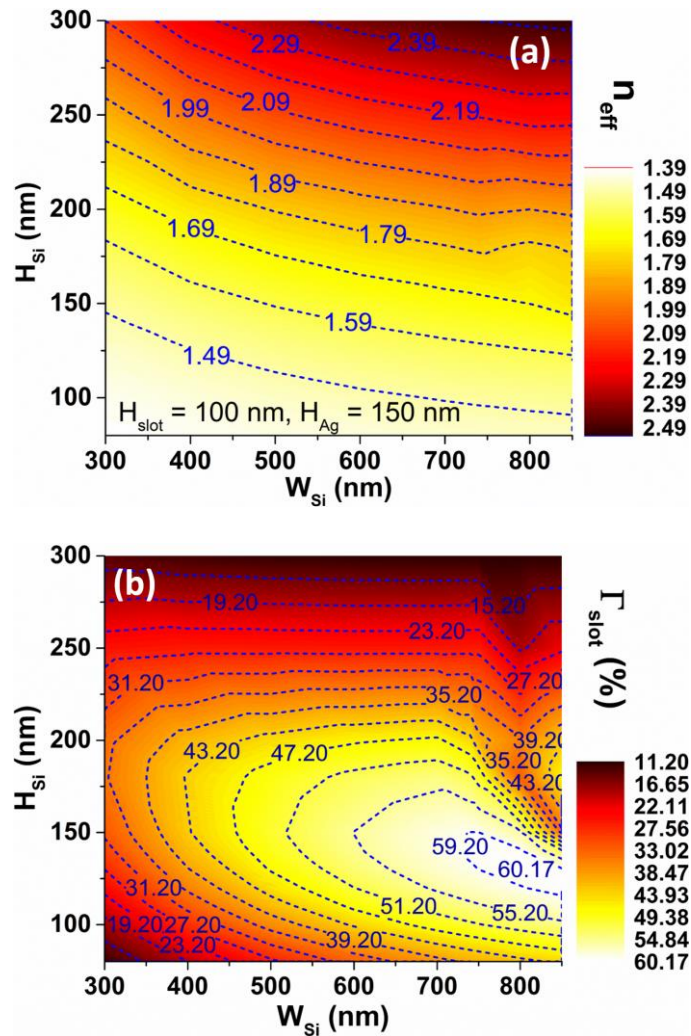


Fig. 5

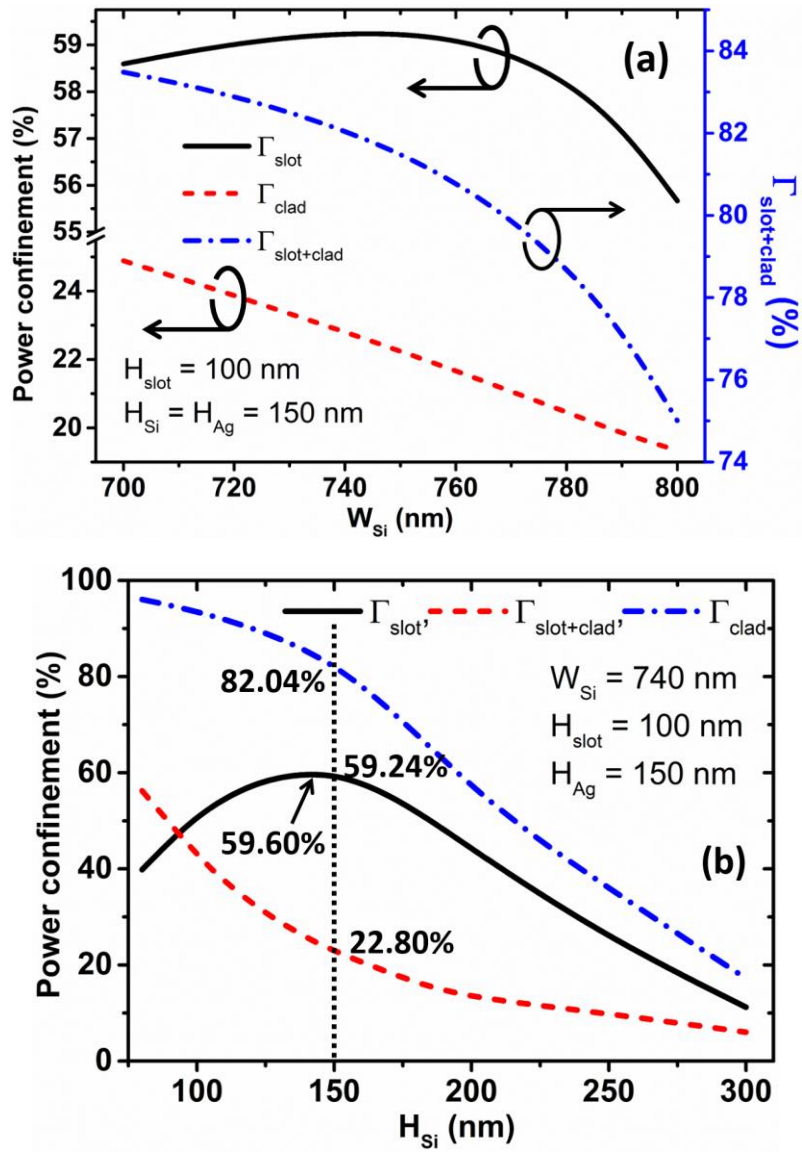


Fig. 6

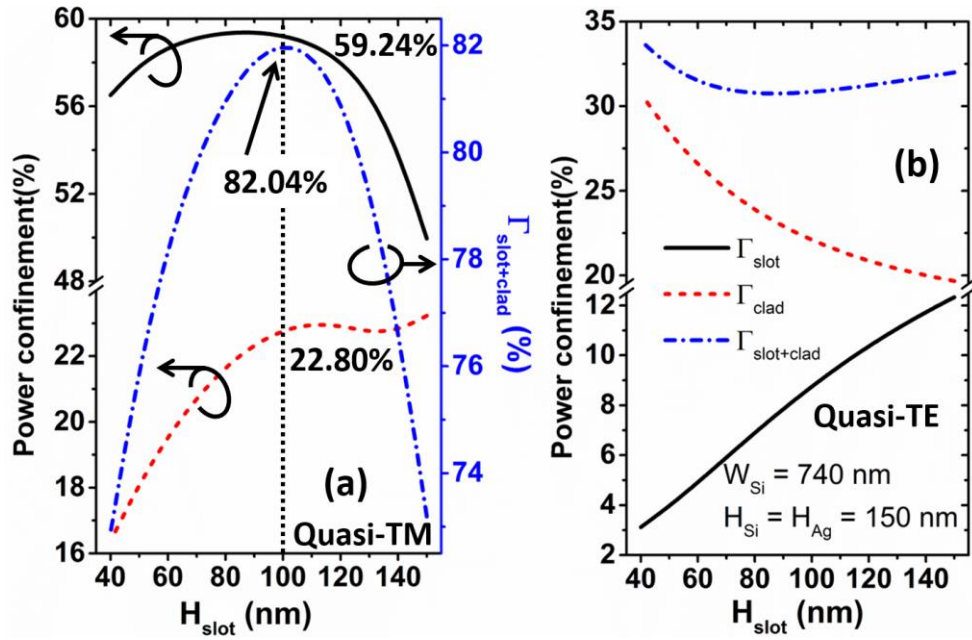


Fig. 7

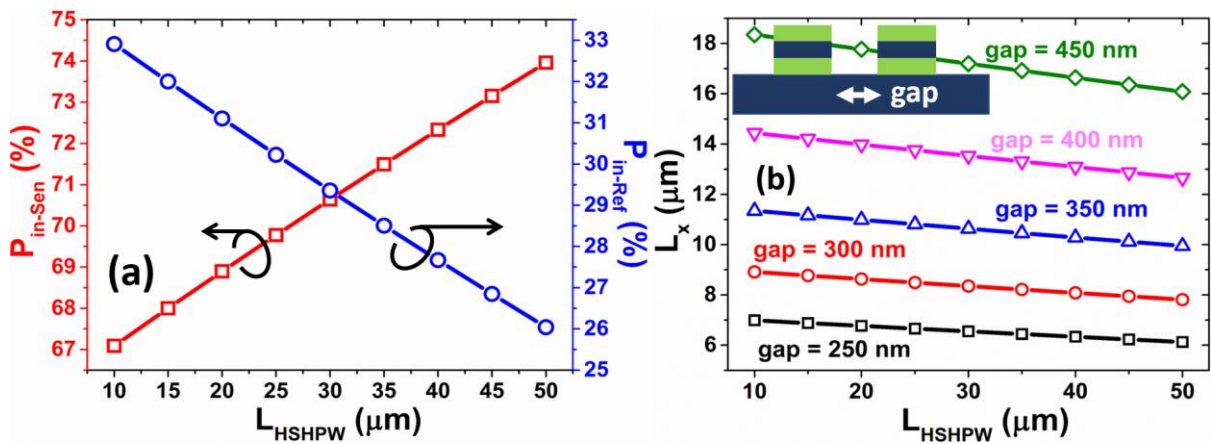


Fig. 8

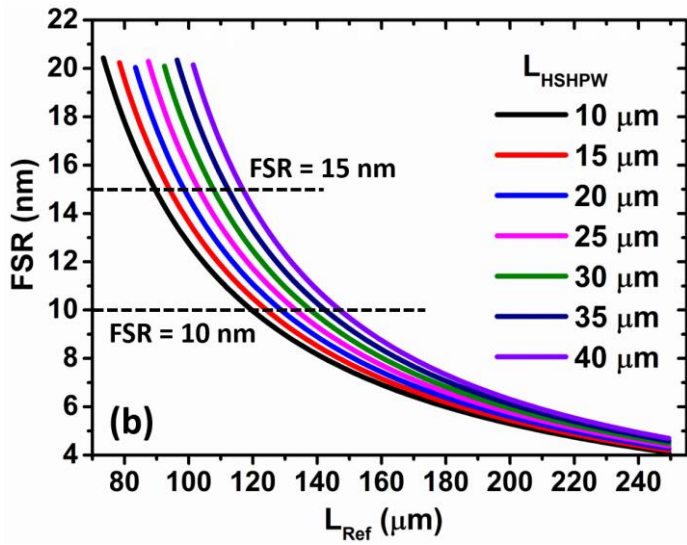
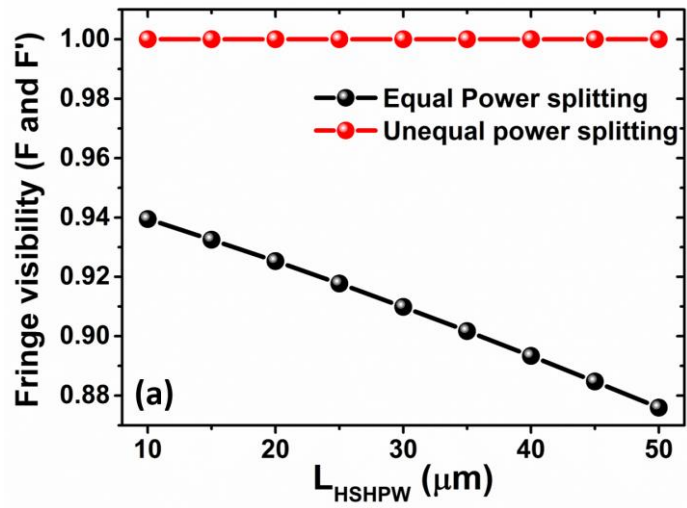


Fig. 9

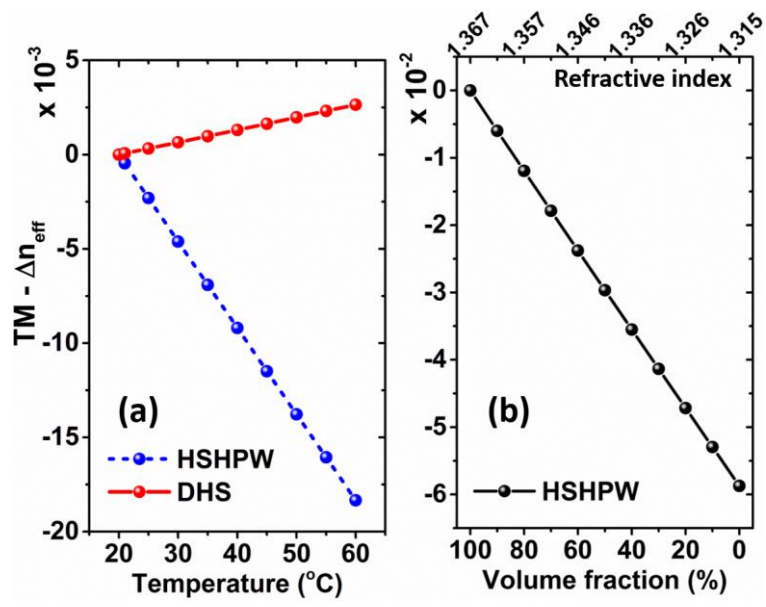


Fig. 10

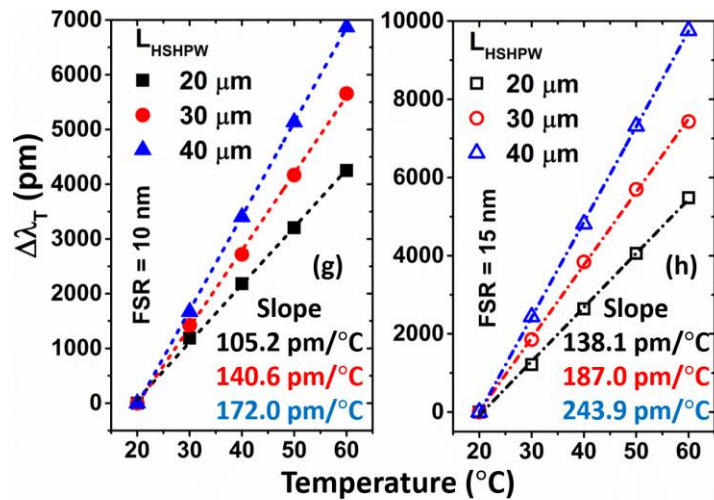
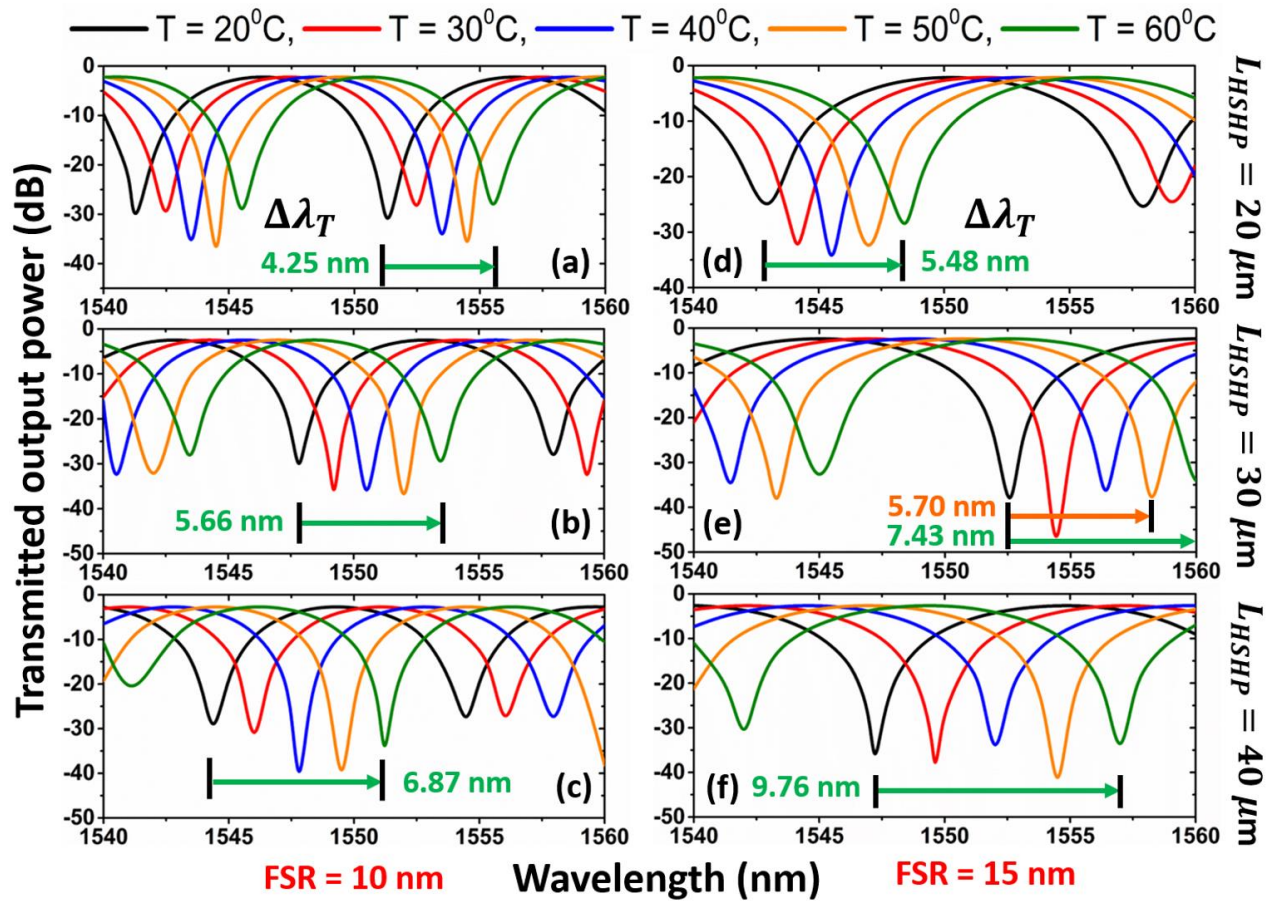


Fig. 11

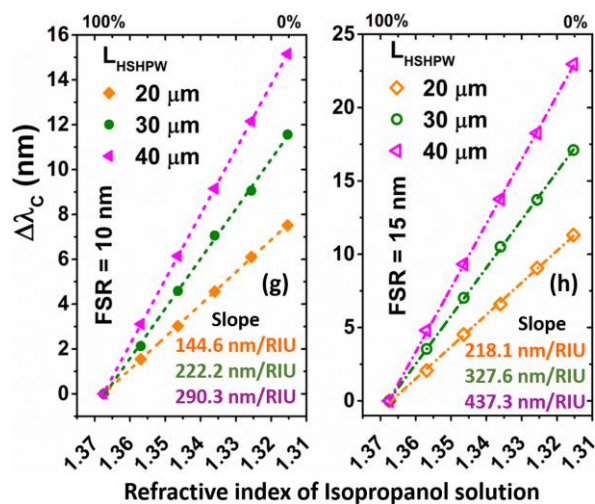
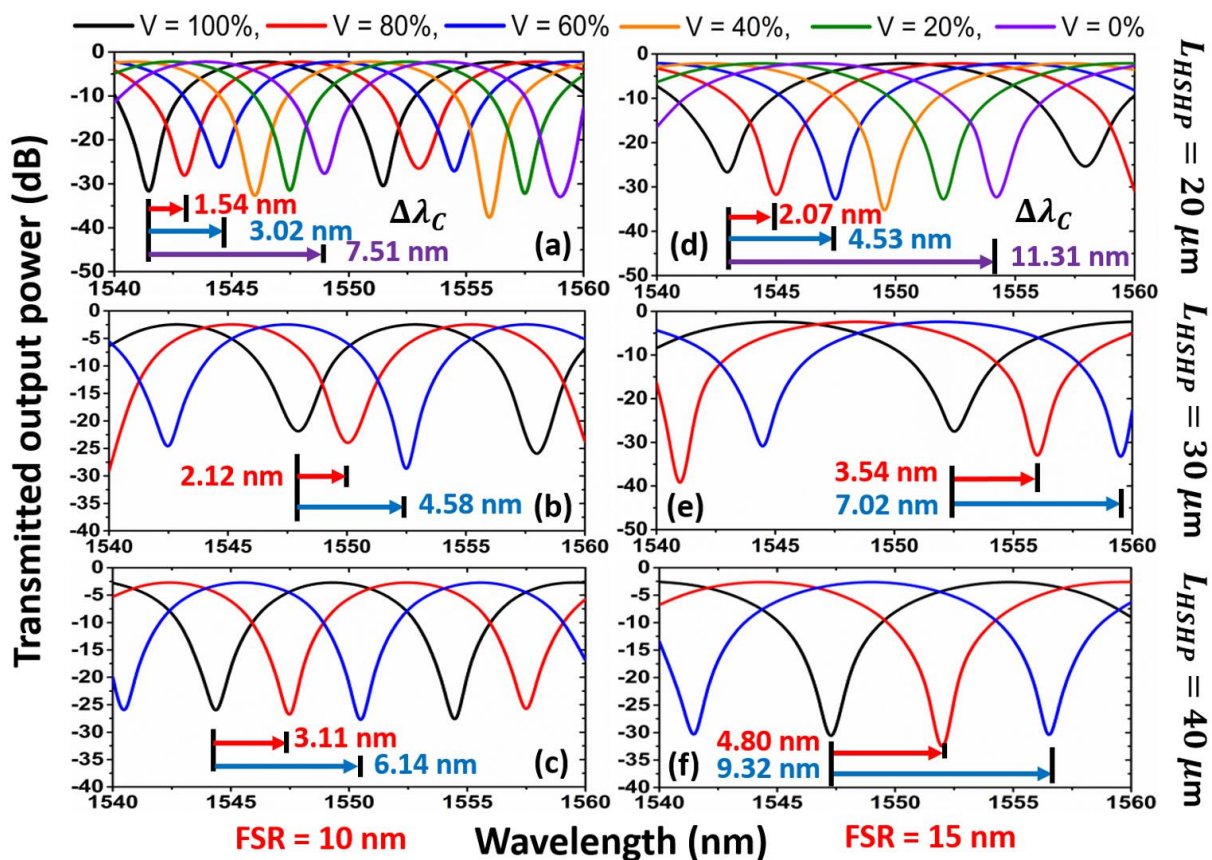


Fig. 12

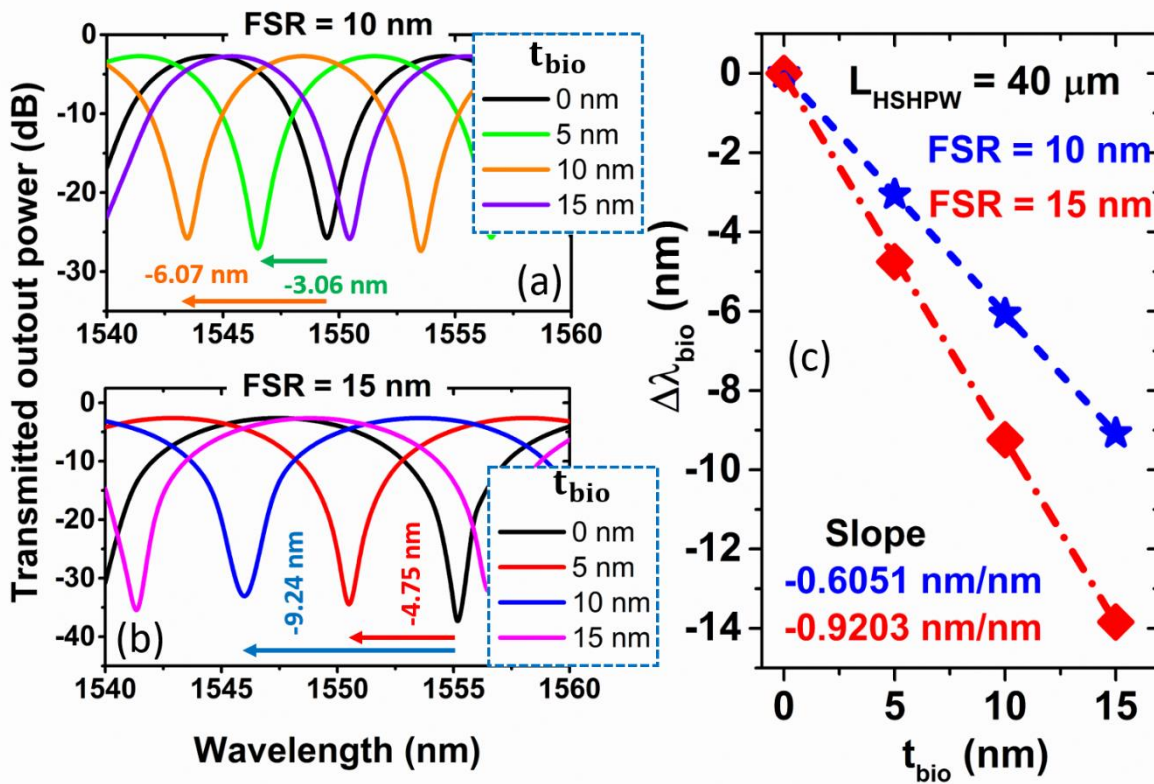


Fig. 13